LANGMUIR

pubs.acs.org/Langmuir Article

Forced Wetting and Dewetting of Water and Oil Droplets on Planar Microfluidic Grids

Xiaoyi Hu, Zhen Wang, David J. Hwang, and Thomas Cubaud*

Cite This: *Langmuir* 2020, 36, 9269–9275 Read Online

ACCESS | Metrics & More | Article Recommendations

ABSTRACT: We experimentally study the wetting behavior of small water and oil droplets spreading and receding from textured surfaces made using a backside laser processing technique. A dual image acquisition system enables the three-dimensional characterization of both wetted area and dynamic contact angles. In particular, we compare droplet growth on smooth surfaces and planar microfluidic grids of various surface coverages and heights and discuss contact angle characterization. The surface texture is shown to trap liquid in microwells during the stick-and-slip motion of advancing contact lines. Receding wetting dynamics of liquid infused substrates shows similarity with forced spreading on smooth surfaces. Contact angle hysteresis is investigated as a function of surface parameters to better delineate specific wetting behaviors of water and oil on laser-processed surfaces.

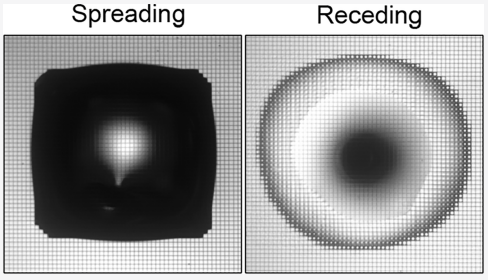

1. INTRODUCTION

The wetting of solid surfaces occurs in many practical situations, including printing and coating processes, as well as in the natural environment where insect legs and plant leaves are often water repellent. While the wetting of ideal surfaces depends on the balance of surface energies,[1−3] most surfaces are chemically heterogeneous and present complex topographies over multiple length scales.[4−6] Spatial discrepancies in shape and composition of solid surfaces, in turn, strongly affect fluid morphology, and natural wetting dynamics typically involves a variety of time scales.[7−9] In addition, the apparent contact angle made between a fluid and a solid displays hysteretic behavior between advancing and receding contact lines and varies with velocity leading to dynamic wetting transitions.[10−12] Wetting properties are also central to fluid transport in porous media, such as during enhanced oil recovery or remediation of contaminated soils, as well as to multiphase flows in microfluidic systems.[13−15] Overall, better understanding the interactions between surface properties and multiphase flows is essential to the development of passive microfluidic phase separators.

Over the years, a vast array of surface modification techniques have been employed to examine wetting properties, including chemical vapor deposition,[16] micropillars,[17] photoresist,[18] grooves,[19] or carbon nanotubes.[20] Advances in surface engineering have also shed light on the advantages of liquid infused surfaces[21−23] to manipulate droplet dynamics and modulate contact angles hysteresis. In general, a fundamental challenge lays in the ability to exploit wetting phenomena and passively drive fluid into a preferential direction by using texture anisotropy and produce capillary rectifiers or liquid diodes.[24,25] Integration of surface modifications into confined microsystems, however, remains challenging in practice, and methods for directly modifying wetting properties inside capillaries are needed. In this context, laser microfabrication techniques[26−30] are promising for inscribing complex patterns in transparent media and present significant advantages due to versatility, cost, and ease of fabrication.

Here, a comprehensive experimental study is conducted to clarify forced spreading and dewetting behaviors of water and oil droplets on laser-patterned surfaces. We first examine the spreading of small droplets fed at constant flow rate on smooth surfaces and discuss the temporal evolution of average contact radius, contact line velocity, advancing contact angle, and shape of wetted area. Smooth surfaces provide a reference to examine the influence of square microfluidic grids of various surface coverages and heights on forced spreading behavior. In particular, the morphology and dynamics of faceted droplets are parametrically investigated with focus on the evolution of advancing contact angles on decorated surfaces. The dewetting process of water droplets is then studied with focus on the evolution of droplet shape, retracting wedge velocity, and apparent receding contact angles. We discuss the analogy between forced spreading on smooth surfaces and dewetting of liquid-impregnated surfaces. Finally, contact angle hysteresis is

Received: May 30, 2020
Revised: July 14, 2020
Published: July 16, 2020

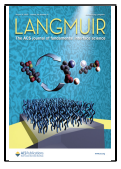

https://dx.doi.org/10.1021/acs.langmuir.0c01601
Langmuir 2020, 36, 9269–9275

related to surface coverage and height of microfluidic grids to unravel selective wetting dynamics between water and oil.

2. METHODS

The experimental apparatus comprises two cameras PixeLINK (PL-B771) with a resolution of 1280 × 1024 pixels and adjustable frame rates for simultaneous observation of bottom and profile views (Figure 1a). A goniometer-based telecentric lens is used for the profile

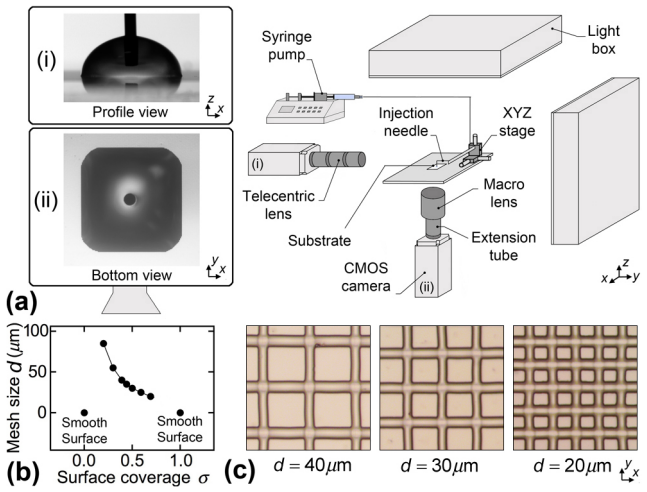

Figure 1. (a) Schematics of experimental setup with profile and bottom views. (b) Substrate characteristics with mesh size d as a function of surface coverage σ. (c) Micrographs of textured surfaces.

view, and a macro lens is employed with an extension tube for the bottom view. Decorated substrates are positioned with grids aligned with the axis of the profile view. A stainless-steel dispensing needle having an internal diameter of 254 μm and outside diameter of 457 μm is mounted on a miniature XYZ stage and connected to a syringe pump to inject and withdraw fluids from substrates at constant flow rate Q = 2 μL/min for both cases. A small flow rate is selected to examine slow spreading and withdrawal processes in the quasi-static regime in the absence of significant viscous or inertial effects. Experiments are conducted at room temperature in ambient air and consist in injecting liquid for about 10 min to probe forced wetting dynamics of sessile drops. Drops are subsequently allowed to relax for 30 min before liquid is withdrawn to examine forced dewetting on microtextured surfaces. Camera frame rates are set between 1 and 3 s per frame to record slow contact line motion at high resolution.

Textured surfaces are fabricated by using a two-photon polymerization technique[31−33] with a picosecond laser having a wavelength of 523 nm and operating at 100 kHz. A thin layer of photopolymer (NOA61 resin) is first spin-coated on borosilicate glass at 6 × 10^3 rpm and then cured under UV light to form an adhesion layer. Another layer of the same photopolymer is then coated at 4 × 10^3 rpm, and mesh patterns are exposed to backside laser focusing at the resin/glass interface. Finally, the substrate is developed and fully cured under a UV lamp.[34−36] Laser scan paths are digitally programmed, and various mesh patterns are fabricated by tuning laser power, speed and number of scans, and focal beam size. This method enables the formation grid patterns of height h = 5 and 9 μm and various square mesh size d = 20, 25, 30, 35, 40, 55, and 85 μm. The laser scanning process introduces a slight dissymmetry between y-lines width w_y = 7.6 μm and x-lines width w_x = 10.1 μm. Therefore, the grid surface coverage fraction is defined as $\sigma = 1 - (d - w_x)(d - w_y)/d^2$ where σ = 0 and 1 correspond to a fully coated surface (Figure 1b). Microsurfaces are inspected for uniformity and produced over an area of 1 cm^2 (Figure 1c). Overall, this method allows us to experimentally interrogate the role of both (x, y)-planar and z-vertical grid patterning on forced wetting and dewetting.

The liquid phases examined in this study are (a) deionized water of viscosity η = 1 mPa s and surface tension γ = 72 mN/m and (b) conventional silicone oil with η = 97 mPa s and γ = 20.9 mN/m. While fluids have widely different characteristic velocities $V^* = \gamma/\eta$, such as 72 m/s for water and 0.22 m/s for the oil, our apparatus allows us to examine advancing and receding contact line velocities on the order of a few μm/s, i.e., for very small capillary numbers $Ca = \eta V/\gamma \sim 10^{-6}$, which indicates a negligible influence of viscosity compared to surface tension on droplet dynamics. In the following, we quantitatively compare forced spreading and dewetting dynamics for both fluids and highlight similar and different aspects on well-defined microfluidic grid patterns.

3. RESULTS AND DISCUSSION

3.1. Forced Wetting of Smooth Surfaces. We first turn our attention to the spreading of water and oil droplets fed at constant flow rate Q on smooth surfaces. Figure 2a displays

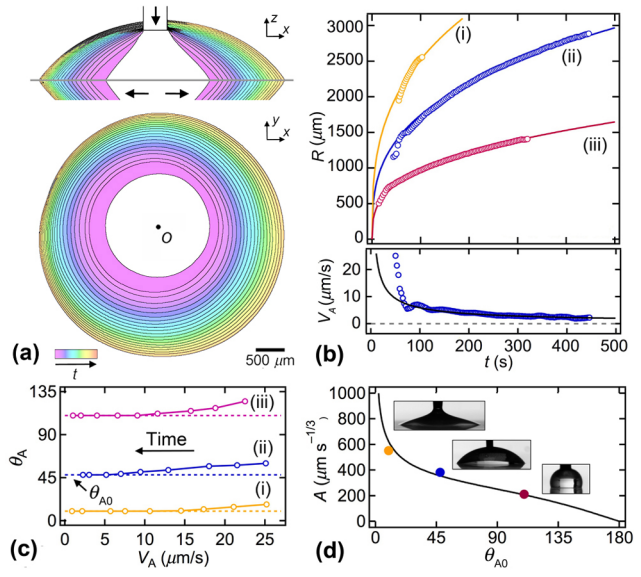

Figure 2. Forced spreading on homogeneous surfaces. (a) Time series of droplet contour for water on photoresist, Δt = 18 s; a spectrum color code is used to highlight evolution of wetted area. (b) Top: time evolution of contact radius R: (i) oil on photoresist, (ii) water on photoresist, and (iii) water on hydrophobic surface. Solid lines: $R = At^{1/3}$ with (i) A = 552, (ii) 382, and (iii) 212 μm $s^{-1/3}$. Bottom: advancing contact line velocity V_A for (ii). (c) Dynamic advancing contact angle θ_A as a function of advancing velocity V_A. (d) Measured growth coefficients A as a function of quasi-static contact angles θ_{A0}. Solid line: spherical cap model for Q = 2 μL/min based on eq 1.

composite images of a time series of both profile and bottom views for the case of a water droplet spreading on photoresist. Parameters of interest include the temporal evolution of advancing contact angles θ_A, interfacial morphology, and wetted area. After the initial contact, droplet shapes are modeled as spherical caps with volume $\Omega = Qt$ and contact angle θ_A. Assuming a spherical cap approximation, the radius R of the wetted area is expected to grow as $R = At^{1/3}$ where the growth coefficient A depends on θ_A and Q according to

$$A = \left[\frac{3\sin^3\theta_A}{\pi(2 - 3\cos\theta_A + \cos^3\theta_A)}Q\right]^{1/3} \quad (1)$$

The contact diameter $D = 2R$ is experimentally measured through spatiotemporal analysis of profile movies, and the time

https://dx.doi.org/10.1021/acs.langmuir.0c01601
Langmuir 2020, 36, 9269−9275

is offset such as $\Omega = 0\ \mu m^3$ for $t = 0$ s. In Figure 2b, droplet radii R on smooth surfaces are fitted with an expression of the form $R = At^{1/3}$ to estimate values of growth coefficient A for (i) oil and (ii) water droplets on flat photoresist surfaces as well as for (iii) a water droplet on a smooth hydrophobic surface. While textured surfaces discussed in this work are made of photoresist, we also include the radius evolution of water spreading on a hydrophobic surface in this section to probe the influence of large contact angles on A in the context of flat surfaces. Overall, modeling of contact radius with $R = At^{1/3}$ shows good agreement with data together with calculations of advancing contact line velocity, $V_A = dR/dt$, which is well fitted with $V_A \sim t^{-2/3}$ for long times $t > 100$ s (Figure 2b, bottom). This result indicates the intrinsic relationship $V \sim R^{-2}$, which is useful for quantifying the forced dewetting process, where time is typically arbitrarily defined, thereby limiting the use of simple scaling approaches based on time. Here, given the low flow rate of injection $Q = 2\ \mu L/min$, the advancing contact line velocity remains on the order of a few micrometers per second for large R. Information about V_A is used to examine the evolution of advancing contact angles θ_A measured from image processing of profile views for each case, and good qualitative agreement is found with the Cox–Voinov[37,38] relationship $\theta_A^3 - \theta_{A0}^3 \sim V_A$, with a cutoff velocity of about 10 μm/s for determining the quasi-static advancing contact angle θ_{A0} on smooth surfaces (Figure 2c). Finally, independent measurements of growth coefficient A and advancing contact angle θ_{A0} compare well with eq 1 as shown in Figure 2d. Quantitative agreement between droplet growth rate and spherical cap model on smooth surfaces indicates that droplet volume loss due to evaporation is negligible compared to the constant added liquid volume during the forced spreading process. This method also shows that growth coefficients A can be used to estimate θ_A via eq 1 over large variations of contact angles from hydrophilic to hydrophobic surfaces. In the following, we extrapolate this approach to the case of textured substrates to compute the equivalent "volumetric" contact angles θ_Ω associated with growth coefficients A of droplets fed at constant flow rate on rough surfaces.

3.2. Spreading on Textured Surfaces. The presence of a microscale grid pattern significantly impacts droplet morphology and spreading dynamics due to the presence of anisotropic surface energy barriers. A typical example of droplet spreading on such surface is represented by using a superposition of contact lines in Figure 3a. The contact line moves row-by-row in a typical zipping mechanism[39] and displays strong stick-and-slip behavior. To obtain additional quantitative insights, it is instructive to plot the temporal evolution of the radii R normal to the four facets, labeled as north, east, south, and west, from the center of injection (Figure 3b). While each radius grows in an apparent random fashion with sudden growth followed by long plateaus, the average radius $R = (R_N + R_E + R_S + R_W)/4$ displays a relatively smooth evolution with a robust scaling relationship of the form $R \sim t^{1/3}$ (Figure 3c) similar to the case of a smooth surface. The stick-and-slip behavior is particularly apparent from the temporal evolution of the advancing contact line velocity V_A, which is characterized with a series of plateaus and spikes corresponding to contact line jumps of one or two rows at a time (Figure 3d). As the droplet spreads on the textured surface, more spikes are observed at early times, showing an overall decrease of velocity as one would expect on a smooth surface where $V_A \sim t^{-2/3}$. Therefore, the presence of the microfluidic grid permits the discretization of contact line

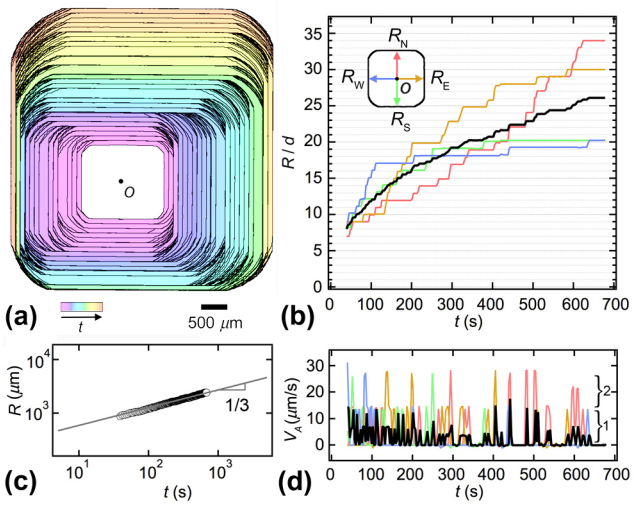

Figure 3. Evolution of water droplet spreading on grid with $d = 85$ μm ($\sigma = 0.2$) and $h = 5$ μm. (a) Time series of droplet contours, $\Delta t = 3$ s; a spectrum color code is used to highlight evolution of wetted area. (b) Evolution of normalized facet radii R/d as a function of time t. (c) Scaling relationship between average radius R and time; solid line: $R \sim t^{1/3}$. (d) Time evolution of advancing velocities V_A showing contact line jumps of one or two rows.

motion in good agreement with continuous motion on a flat surface.

Measurements of quasi-static advancing contact angle θ_{A0} on textured surfaces are conducted in a similar fashion to smooth surfaces. Because of stick-and-slip motion, however, reported values correspond to the average maximum angle detected before local contact line motion is observed from profile movies (Figures 4a,b). For water–air systems, the apparent

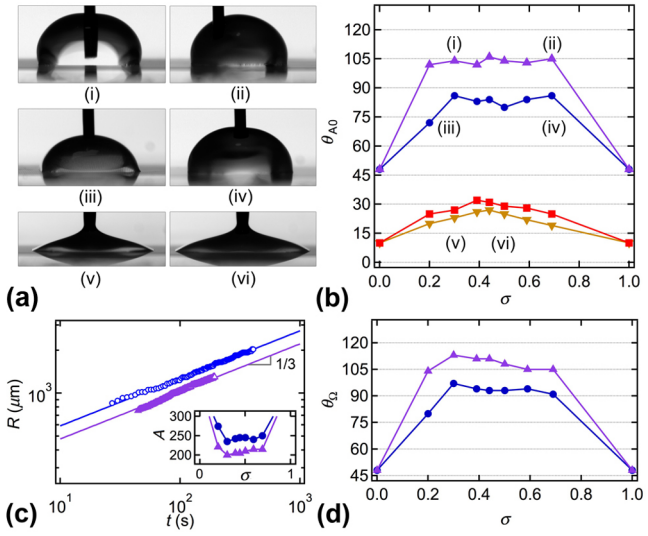

Figure 4. Advancing and volumetric contact angles on textured surfaces. (a) Micrograph of profile views: from (i) to (iv), water droplet; (v) and (vi), oil droplets. Evolution of average advancing contact angle θ_{A0} as a function of surface coverage σ; water droplet, $h = 5$ (●) and 9 μm (▲); oil droplet, $h = 5$ (■) and 9 μm (▼); (i) to (vi) correspond to the case shown in (a). (c) Temporal evolution of contact radius R for water with $\sigma = 0.2$, $h = 5$ (○) and 9 μm (△). Inset: measurement of growth coefficient A for water. (d) Evolution of water volumetric contact angles θ_Ω vs grid coverage σ, $h = 5$ (●) and 9 μm (▲).

https://dx.doi.org/10.1021/acs.langmuir.0c01601
Langmuir 2020, 36, 9269–9275

contact angle strongly depends on the height h of the grid pattern with a marked increase for larger h. By contrast, while the contact angle on textured surfaces is larger compared to that of a smooth surface for oil in air, an increase in h produces a slightly smaller contact angle. In both cases, the range of variation of θ_{A0} with σ is rather narrow, suggesting a limited influence of surface coverage σ compared to the height h of microgrids.

The transition from partial wetting $\theta_{A0} < \pi/2$ for water droplets on surfaces with $h = 5$ μm to partial nonwetting $\theta_{A0} > \pi/2$ for water droplets on surfaces having $h = 9$ μm indicates a change of sign of cos θ_{A0}, which limits the use of Wenzel law in our situation. This discrepancy is, in part, due to the fact that droplets are mainly confined with rows and θ_{A0} correspond to apparent contact angles measured from large-scale deformation of the liquid−air interface at the solid surface while smaller liquid wedges can be seen extruding from droplets at a smaller scale. As a result, direct contact angle measurements from profile views typically involve an uncertainty of ±3°, which roughly corresponds to the size of symbols used in Figure 4b. This measurement is based on the assumption that actual, local contact angles on the textured surface control the overall shape of the free liquid−air surface from which an apparent contact angle θ_{A0} as well as an average spreading parameter[40] can be defined. In addition, stick-and-slip motion and the development of facets and corners in the wetted area suggest contact angle variations along the contact line, which limits interpretation of θ_{A0}. Hence, we also examine the evolution of the growth coefficient A for water droplets on textured surfaces (Figure 4c) to calculate equivalent volumetric contact angles θ_Ω (Figure 4d) and examine droplet average behavior. While a very similar trend is found between θ_{A0} and θ_Ω, volumetric angles are larger than advancing angles with a ratio $\theta_\Omega/\theta_{A0} \sim 1.1$. Indeed, θ_Ω is based on the volume of a spherical cap having uniform contact radius R, whereas square-shaped droplets have an average R based on distance from facets. Therefore, faceted droplets can sustain larger liquid volumes for similar R due to the presence of corners. In turn, microfluidic grids offer the possibility to confine larger amount of liquid in the form of faceted drops compared to smooth surfaces having droplets with spherical caps, as indicated by the wide increase of volumetric contact angles θ_Ω from flat to meshed surfaces.

We now examine the morphology of contact lines on textured substrates using the bottom view. Figure 5a displays various time series of droplet spreading on grid patterns. While it is found that some droplets appear to favor certain flow directions, which could result from a variety of factors, such as slight horizontal inclination of the substrate, small vertical misalignment of injection needle, or interfacial deformation due to fluid attachment, the overall shape of the wetted area remains consistent for a parametric study. For the oil−air system, droplets quickly spread to a contact radius R of about 1.5 mm before adopting the typical stick-and-slip behavior of faceted droplet. For water−air systems, the larger contact angle allows for capturing dynamics starting with a radius R of about 0.5 mm. A parameter of interest consists in the aspect ratio Γ of droplets defined as the ratio of the length-to-width of droplet. Here, the length is defined as the larger lateral extension and the width the smaller breadth of the droplet. The length and width are individually selected for each droplet to define an aspect ratio Γ larger than unity. The spatial evolution of Γ as a function of R is shown in Figure 5b for the

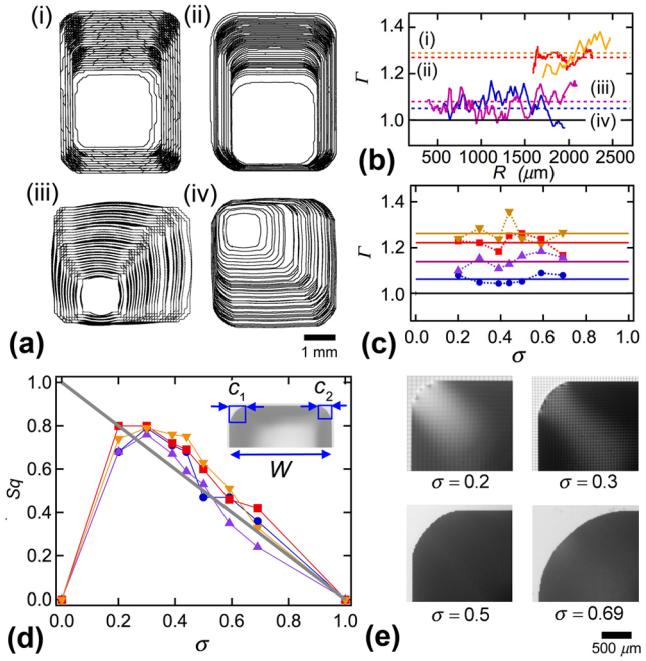

Figure 5. Droplet morphology on patterned substrates. (a) Composite image of droplet contours. Oil droplet: (i) $\sigma = 0.2$, $h = 9$ μm, and (ii) $\sigma = 0.34$, $h = 5$ μm. Water droplet: (iii) $\sigma = 0.2$, $h = 9$ μm, and (iv) $\sigma = 0.34$, $h = 5$ μm. (b) Spatial evolution of droplet aspect ratio Γ for cases shown in (a). (c) Influence of surface coverage σ on average aspect ratio for water with Γ = 1.06 for $h = 5$ μm (●) and 1.14 for $h = 9$ μm (▲) and for oil with Γ = 1.22 for $h = 5$ μm (■) and 1.26 for $h = 9$ μm (▼). (d) Evolution of droplet squareness Sq vs coverage fraction σ. Symbols identical to (c). Solid gray line: $Sq = 1 - \sigma$. (e) Bottom view micrographs of oil droplet corners for with $h = 5$ μm.

four typical cases associated with Figure 5a. Owing to the slight dissymmetry of the length and width in the thickness of the patterned grid, the aspect ratio typically increased with h and is significantly more marked for the oil−air system. This behavior is interpreted as a result of a weaker surface tension γ for oil−air systems compared to water−air systems, which tend to more strongly minimize the interfacial area. While the aspect ratio fluctuates for a given droplet, the average values of Γ across all surfaces show similar behavior (Figure 5c).

In addition to the aspect ratio Γ, the shape of droplets can also be characterized with their degree of "squareness" Sq that we define as $Sq = 1 - 2\sum c_i/\sum W_i$, where c_i is the length of a droplet corner and W_i is the distance between two facets i. Here, this parameter is developed for the characterization of droplet spreading on square grid patterns by analogy with the roundness, which is based on the ratio of area-to-perimeter but lacks specificity. As the squareness $Sq = 1$ for a rectangle and $Sq = 0$ for a circle, this parameter is employed to quantify the degree of droplet compliance with the imposed surface geometry. By contrast to the advancing contact angle θ_A and droplet aspect ratio Γ, the squareness is strongly affected by the grid patterns for both water and oil droplets, which display similar behavior that is reasonably well fit with the expression $Sq = 1 - \sigma$, independently of h as can be seen in Figures 5d,e. This work shows that for a given square grid the shape of a forced spreading droplet becomes more strongly deformed with the grid size d.

3.3. Dewetting of Patterned Surfaces. In this section, we examine forced dewetting processes and study the

https://dx.doi.org/10.1021/acs.langmuir.0c01601
Langmuir 2020, 36, 9269−9275

dynamics of receding contact lines on liquid-impregnated surfaces. The wetting dynamics associated with liquid suction from textured surfaces significantly differs from those observed during the injection process. Once droplets are formed and allowed to relax for 30 min, the direction of syringe pump is inverted with a constant flow rate of suction of $Q = 2\ \mu$L/min. During the relaxation period, the droplet volume is expected to slightly decrease due to evaporation thereby limiting analysis based on absolute droplet volume and focus is on contact line motion. During the first stage of droplet withdrawal, contact lines remain pinned until the quasi-static receding contact angle θ_{R0} is reached as displayed in the time series of the droplet profile in Figure 6a during t_0 and t_1. Owing to a large

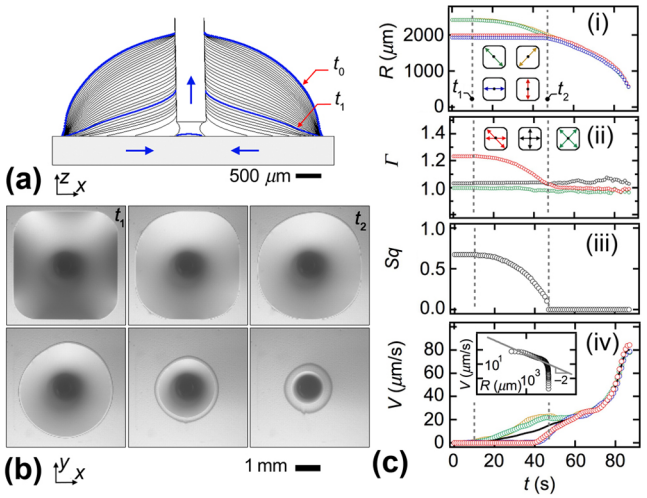

Figure 6. Example of dewetting dynamics for a water droplet on grid pattern with $d = 35\ \mu$m and $h = 5\ \mu$m (arbitrary time offset). (a) Composite time series of droplet withdraw process ($\Delta t = 12$ s) with pinned contact line for $t < t_1$ and a receding contact line for $t > t_1$. (b) Bottom view micrographs show morphological changes of wetted area with circular contact line for $t > t_2$. (c) Temporal modification of shape parameters: (i) evolution of horizontal, vertical, and diagonal radii as indicated with icons, (ii) change of aspect ratios Γ, (iii) reduction of droplet squareness, and (iv) temporal evolution of receding wedge velocity V. Inset: V vs R. Solid line: $V = 3.5 \times 10^7 R^{-2}$.

contact angle hysteresis of rough surfaces, most of the droplet volume becomes depleted during this period. When the receding contact angle θ_{R0} is reached, the second stage consists in a progressive retraction of the wetted surface toward the suction needle until a small capillary bridge is formed and eventually breaks, leaving a small droplet on the surface. Given the surfaces investigated in this work, the second stage is only observed with water droplet as oil leaves a thin film on photoresist-textured surfaces. Figure 6b documents micrographs of the bottom view of the retraction stage, which can be decomposed into two phases with first the evolution of the wetted area from a square to a circular region between t_1 and t_2 followed with a uniform reduction of the wetted area from the substrate. While advancing contact lines are characterized with a significant stick and slip, the receding motion on liquid infused surfaces remains smooth as can be seen in Figure 6ci with the temporal evolution of horizontal, vertical, and diagonal half-width R of the wetted area. The geometrical change of wetted area from a square-like to a circular shape is particularly smooth as revealed with the evolution of various droplet aspect ratios (Figure 6ci) as well as the squareness Sq (Figure 6cii). In terms of dynamics, while the contact line remains pinned at the facets and evolves in the corners during the first stage, computing the average wedge velocity V shows a smooth increase with time. Here, we distinguish the liquid wedge region (liquid−liquid−gas) from the triple line region (i.e., liquid−solid−gas) since the forced dewetting process imposes a large bulk wedge velocity V near the suction needle in excess of the natural dewetting velocity V_R and a thin film is left on the textured surface. Therefore, while the wetted area and wedge area coincide at the early stage of liquid withdrawal, areas dissociate in the final stage. Here, we focus on the wedge area and compute the temporal evolution of the average wedge radius R from measurements (Figure 6ciii). Because no initial time can be meaningfully measured in the dewetting process, we compare V to the wedge radius and find the intrinsic relationship $V \sim R^{-2}$, which shows that besides droplet morphological differences, forced spreading on smooth surfaces and forced dewetting on liquid-infused surfaces display similar behaviors, which are essentially controlled with the externally imposed flow rate.

The forced withdrawal process imposes significant constraint on the contact angle. As the velocity increases near the needle, the receding contact angle θ_R decreases until it becomes null and some liquid remains trapped in microscale wells formed by the textured surface. As a result, one needs to part the contact angle θ_R and the angle θ_W of the main liquid wedge, where most of the liquid is contained (Figure 7a). While for oil, a thin film remains constantly trapped; in the case of water, evaporation patterns are observed with complex variations of

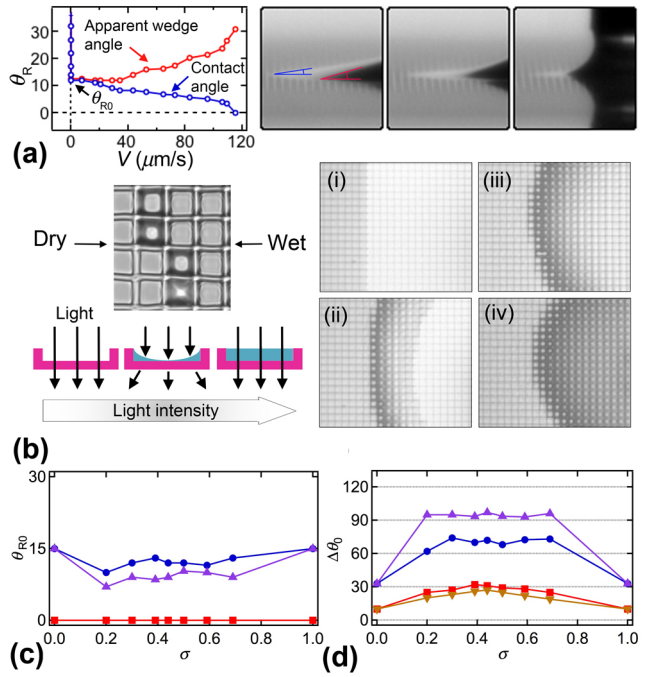

Figure 7. Receding contact lines on inhibited microgrid patterns. (a) Left: evolution of contact and wedge angles of water for $d = 35\ \mu$m and $h = 5\ \mu$m with receding velocity V. Right: time series of profile views. (b) Top: bottom micrograph of contact area for water with $d = 85\ \mu$m and $h = 5\ \mu$m. Bottom: schematics of light intensity based on well filling. Right: time series of receding water droplet with for $d = 85\ \mu$m and $h = 5\ \mu$m. (c) Evolution of receding contact angle θ_{R0} with surface coverage. (d) Quasi-static apparent contact angle hysteresis on grid patterned surfaces.

https://dx.doi.org/10.1021/acs.langmuir.0c01601
Langmuir 2020, 36, 9269−9275

recorded light intensity in the bottom view (Figure 7b). The thin film retraction process is expected to depend on evaporation due to the large specific area and small liquid volume of the thin film. Evaporation patterns are typically observed with water at later times. Here, we discuss contact line motion in the first instants of the retraction process. Overall, the quasi-static receding contact angle θ_{R0} is measured at the beginning of the withdrawal process when V remains below 20 μm/s, and no significant influence of surface coverage σ is observed. We note, however, a slight influence of the pattern height h with smaller receding contact angles θ_{R0} for larger h in the case of water and $\theta_R = 0$ for oil regardless of coverage or height (Figure 7c). As a result, the quasi-static contact angle hysteresis $\Delta\theta_0 = \theta_{A0} - \theta_{R0}$ is much larger for water compared to oil on liquid-infused surfaces showing significant differences between water and oil wetting properties.

4. CONCLUSIONS

In this work, we examine the advancing and receding wetting dynamics of water and oil droplets on plane microfluidic grids fabricated using an original backside laser processing technique. During the forced spreading process, water and oil droplets display strong stick-and-slip behavior with wetted areas adopting similar shapes despite large differences in apparent contact angles. We analyze the growth rate of various droplets fed at constant flow rate on smooth surfaces and develop a simple model to predict volumetric contact angles of spherical caps. This approach is applied to forced spreading of droplets on patterned surfaces to estimate equivalent volumetric contact angles, which are found in slight excess of locally measured contact angles due to complex shape of faceted droplets on microgrids. This method permits the determination of an average droplet contact angle in the context of a contact line having spatially varying contact angles. The role of surface coverage and height of continuous textures on contact angle hysteresis is independently determined, and various shape parameters, including droplet aspect ratio and squareness, are measured to quantitatively characterize faceted droplet growth on textured surfaces. Forced receding wetting dynamics of rough surfaces considerably differs from that of spreading due to liquid infusion of microwells and interplay between natural dewetting behavior, evaporation, and forced liquid withdrawal.

Overall, this work shows the discretization of contact line motion using external flow control on patterned substrates. While this study characterizes the phenomenology of droplets fed and withdrew at small flow rates on grids having fixed thickness and various mesh sizes, further work could investigate the role of larger flow rates as well as the influence of ordered and disordered patterns on chemically heterogeneous surfaces. Other aspects of interest include investigations of wetting-induced deformations of soft substrates and characterization of hysteresis cycles to better delineate droplet deposition and removal from textured surfaces under various conditions of temperature and humidity. Microengineered surfaces are useful to produce specific interfacial dynamics for water and oil phases using bulk flow manipulations. Future work also includes examination of liquid/liquid wetting characteristics on microfluidic grids in both unbounded and confined microfluidic systems to improve understanding of water/oil dynamics in miniature devices having surface modifications for the design of passive liquid phase separators at the small scale.

AUTHOR INFORMATION

Corresponding Author

Thomas Cubaud − *Department of Mechanical Engineering, Stony Brook University, Stony Brook, New York 11794, United States;* orcid.org/0000-0002-9296-0783; Email: thomas.cubaud@stonybrook.edu

Authors

Xiaoyi Hu − *Department of Mechanical Engineering, Stony Brook University, Stony Brook, New York 11794, United States*

Zhen Wang − *Department of Mechanical Engineering, Stony Brook University, Stony Brook, New York 11794, United States*

David J. Hwang − *Department of Mechanical Engineering, Stony Brook University, Stony Brook, New York 11794, United States;* orcid.org/0000-0002-9928-1484

Complete contact information is available at: https://pubs.acs.org/10.1021/acs.langmuir.0c01601

Notes

The authors declare no competing financial interest.

ACKNOWLEDGMENTS

We have appreciated discussions with Carlos Colosqui and Dhiraj Nandyala. This material is based upon work supported by the National Science Foundation under Grant CBET-1605809.

REFERENCES

(1) de Gennes, P. G. Wetting - statics and dynamics. *Rev. Mod. Phys.* **1985**, *57*, 827.

(2) Israelachvili, J. *Intermolecular and Surface forces*; Academic Press: Amsterdam, 1991.

(3) Adamson, A. W.; Gast, A. P. *Physical Chemistry of Surfaces.*; John Wiley & Sons, Inc.: New York, 1991.

(4) Herminghaus, S.; Brinkmann, M.; Seemann, R. Wetting and dewetting of complex surface geometries. *Annu. Rev. Mater. Res.* **2008**, *38*, 101.

(5) Quéré, D. Wetting and roughness. *Annu. Rev. Mater. Res.* **2008**, *38*, 71.

(6) Savva, N.; Groves, D.; Kalliadasis, S. Droplet dynamics on chemically heterogeneous substrates. *J. Fluid Mech.* **2019**, *859*, 321.

(7) Snoeijer, J. H.; Andreotti, B. Moving contact lines: Scales, regimes, and dynamical transitions. *Annu. Rev. Fluid Mech.* **2013**, *45*, 269.

(8) Seveno, D.; Blake, T. D.; Goossens, S.; De Coninck, J. Predicting the wetting dynamics of a two-liquid system. *Langmuir* **2011**, *27*, 14958.

(9) Jose, B. M.; Nandyala, D.; Cubaud, T.; Colosqui, C. E. Physical ageing of spreading droplets in a viscous ambient phase. *Sci. Rep.* **2018**, *8*, 14159.

(10) Blake, T. D.; Ruschak, K. J. A maximum speed of wetting. *Nature* **1979**, *282*, 489.

(11) Quéré, D. Fluid coating on a fiber. *Annu. Rev. Fluid Mech.* **1999**, *31*, 347.

(12) Snoeijer, J. H.; Delon, G.; Fermigier, M.; Andreotti, B. Avoided critical behavior in dynamically forced wetting. *Phys. Rev. Lett.* **2006**, *96*, 174504.

(13) Cottin, C.; Bodiguel, H.; Colin, A. Influence of wetting conditions on drainage in porous media: A microfluidic study. *Phys. Rev. E* **2011**, *84*, 026311.

(14) Jose, B. M.; Cubaud, T. Formation and dynamics of partially wetting droplets in square microchannels. *RSC Adv.* **2014**, *4*, 14962.

(15) Lu, N. B.; Browne, C. A.; Amchin, D. B.; Nunes, J. K.; Datta, S. S. Controlling capillary fingering using pore size gradients in disordered media. *Phys. Rev. Fluids* **2019**, *4*, 084303.
(16) Chaudhury, M. K.; Whitesides, G. M. How to make water run huphill. *Science* **1992**, *256*, 1539.
(17) Bico, J.; Tordeux, C.; Quéré, D. Rough wetting. *Eur. Phys. Lett.* **2001**, *55*, 214.
(18) Cubaud, T.; Fermigier, M. Advancing contact lines on chemically patterned surfaces. *J. Colloid Interface Sci.* **2004**, *269*, 171.
(19) Wang, D.; Jiang, Y.; Zhu, Z.; Yin, W.; Asawa, K.; Choi, C.-H.; Drelich, J. W. Contact Line and Adhesion Force of Droplets on Concentric Ring- Textured Hydrophobic Surfaces. *Langmuir* **2020**, *36*, 2622.
(20) Busà, C.; Rickard, J. J. S.; Chun, E.; Chong, Y.; Navaratnam, V.; Oppenheimer, P. G. Tunable superapolar Lotus-to-Rose hierarchical nanosurfaces via vertical carbon nanotubes driven electrohydrodynamic lithography. *Nanoscale* **2017**, *9*, 1625.
(21) Guan, J. H.; Wells, G. G.; Xu, B.; McHale, G.; Wood, D.; Martin, J.; Stuart-Cole, S. Evaporation of Sessile Droplets on Slippery Liquid-Infused Porous Surfaces (SLIPS). *Langmuir* **2015**, *31*, 11781.
(22) Semprebon, C.; McHale, G.; Kusumaatmaja, H. Apparent contact angle and contact angle hysteresis on liquid infused surfaces. *Soft Matter* **2017**, *13*, 101.
(23) Wells, G. G.; Ruiz-Gutiérrez, E.; Le Lirzin, Y.; Nourry, A.; Orme, B. V.; Pradas, M.; Ledesma-Aguilar, R. Snap evaporation of droplets on smooth topographies. *Nat. Commun.* **2018**, *9*, 1380.
(24) Li, J.; Zhou, X.; Li, J.; Che, L.; Yao, J.; McHale, G.; Chaudhury, M. K.; Wang, Z. Topological liquid diode. *Sci. Adv.* **2017**, *3*, No. eaao3530.
(25) Comanns, P.; Buchberger, G.; Buchsbaum, A.; Baumgartner, R.; Kogler, A.; Bauer, S.; Baumgartner, W. Directional, passive liquid transport: the Texas horned lizard as a model for a biomimetic 'liquid diode'. *J. R. Soc., Interface* **2015**, *12*, 20150415.
(26) Stratakis, E.; Ranella, A.; Fotakis, C. Biomimetic micro/nanostructured functional surfaces for microfluidic and tissue engineering applications. *Biomicrofluidics* **2011**, *5*, 013411.
(27) Sugioka, K.; Cheng, Y. Ultrafast lasers—reliable tools for advanced materials processing. *Light: Sci. Appl.* **2014**, *3*, No. e149.
(28) Davis, E.; Liu, Y.; Jiang, L.; Lu, Y.; Ndao, S. Wetting characteristics of 3-dimensional nanostructured fractal surfaces. *Appl. Surf. Sci.* **2017**, *392*, 929.
(29) Malinauskas, M.; Žukauskas, A.; Hasegawa, S.; Hayasaki, Y.; Mizeikis, V.; Buividas, R.; Juodkazis, S. Ultrafast laser processing of materials: from science to industry. *Light: Sci. Appl.* **2016**, *5*, No. e16133.
(30) Wang, Q.; Samanta, A.; Shaw, S. K.; Hu, H.; Ding, H. Nanosecond laser-based high-throughput surface nanostructuring (nHSN). *Appl. Surf. Sci.* **2020**, *507*, 145136.
(31) Kawata, S.; Sun, H.-B.; Tanaka, T.; Takada, K. Finer features for functional microdevices. *Nature* **2001**, *412*, 697.
(32) Cumpston, B. H.; Ananthavel, S. P.; Barlow, S.; Dyer, D. L.; Ehrlich, J. E.; Erskine, L. L.; Heikal, A. A.; Kuebler, S. M.; Lee, I.-Y. S.; McCord-Maughon, D.; Qin, J.; Röckel, H.; Rumi, M.; Wu, X.-L.; Marder, S. R.; Perry, J. W. Two-photon polymerization initiators for three-dimensional optical data storage and microfabrication. *Nature* **1999**, *398*, 51.
(33) Yan, D.; Chang, J.; Zhang, H.; Liu, J.; Song, H.; Xue, Z.; Zhang, F.; Zhang, Z. Soft three-dimensional network materials with rational bio-mimetic designs. *Nat. Commun.* **2020**, *11*, 1180.
(34) Jeon, H.; Hidai, H.; Hwang, D. J.; Grigoropoulos, C. P. Fabrication of arbitrary polymer patterns for cell study by two-photon polymerization process. *J. Biomed. Mater. Res., Part A* **2009**, *9999A*, 56.
(35) Jeon, H.; Hidai, H.; Hwang, D. J.; Healy, K. E.; Grigoropoulos, C. P. The effect of micronscale anisotropic cross patterns on fibroblast migration. *Biomaterials* **2010**, *31*, 4286.
(36) Cheng, D.; Jayne, R. K.; Tamborini, A.; Eyckmans, J.; White, A. E.; Chen, C. S. Studies of 3D directed cell migration enabled by direct laser writing of curved wave topography. *Biofabrication* **2019**, *11*, 021001.
(37) Voinov, O. V. Hydrodynamics of wetting. *Fluid Dyn.* **1977**, *11*, 714.
(38) Cox, R. G. Inertial and viscous effects on dynamic contact angles. *J. Fluid Mech.* **1998**, *357*, 249.
(39) Cubaud, T.; Fermigier, M. Faceted drops on heterogeneous surfaces. *Europhys. Lett.* **2001**, *55*, 239.
(40) Andrieu, C.; Sykes, C.; Brochard, F. Average spreading parameter on heterogeneous surfaces. *Langmuir* **1994**, *10*, 2077.

https://dx.doi.org/10.1021/acs.langmuir.0c01601
Langmuir 2020, 36, 9269−9275